Published in final edited form as:
J Am Chem Soc. 2004 June 23; 126(24): 7486–7495. doi:10.1021/ja038218j.

Single Crystal X- and Q-Band EPR Spectroscopy of a Binuclear Mn_2(III,IV) Complex Relevant to the Oxygen-Evolving Complex of Photosystem II

Junko Yano[*,†,‡], **Kenneth Sauer**[†,‡], **Jean-Jacques Girerd**[§], and **Vittal K. Yachandra**[*,†]
Melvin Calvin Laboratory, Physical Biosciences Division, Lawrence Berkeley National Laboratory, Berkeley, California 94720, Department of Chemistry, University of California, Berkeley, California 94720-5230, and Laboratoire de Chimie Inorganique, UMR 8613, Institut de Chimie Moléculaire d'Orsay, Université Paris XI, F-91405 Orsay Cedex, France

[†] Physical Biosciences Division, Lawrence Berkeley National Laboratory.

[‡] Department of Chemistry, University of California, Berkeley.

[§] Laboratoire de Chimie Inorganique, Institut de Chimie Moléculaire d'Orsay, Université Paris XI, Orsay Cedex, France.

Abstract

The anisotropic g and hyperfine tensors of the Mn di-μ-oxo complex, $[Mn_2(III,IV)O_2(phen)_4](PF_6)_3{\cdot}CH_3CN$, were derived by single-crystal EPR measurements at X- and Q-band frequencies. This is the first simulation of EPR parameters from single-crystal EPR spectra for multinuclear Mn complexes, which are of importance in several metalloenzymes; one of them is the oxygen-evolving complex in photosystem II (PS II). Single-crystal $[Mn_2(III,IV)O_2(phen)_4](PF_6)_3{\cdot}CH_3CN$ EPR spectra showed distinct resolved ^{55}Mn hyperfine lines in all crystal orientations, unlike single-crystal EPR spectra of other Mn_2(III,IV) di-μ-oxo bridged complexes. We measured the EPR spectra in the crystal *ab*- and *bc*-planes, and from these spectra we obtained the EPR spectra of the complex along the unique *a*-, *b*-, and *c*-axes of the crystal. The crystal orientation was determined by X-ray diffraction and single-crystal EXAFS (Extended X-ray Absorption Fine Structure) measurements. In this complex, the three crystallographic axes, *a*, *b*, and *c*, are parallel or nearly parallel to the principal molecular axes of $Mn_2(III,IV)O_2(phen)_4$ as shown in the crystallographic data by Stebler et al. (*Inorg. Chem.* **1986**, *25*, 4743). This direct relation together with the resolved hyperfine lines significantly simplified the simulation of single-crystal spectra in the three principal directions due to the reduction of free parameters and, thus, allowed us to define the magnetic **g** and **A** tensors of the molecule with a high degree of reliability. These parameters were subsequently used to generate the solution EPR spectra at both X- and Q-bands with excellent agreement. The anisotropic g and hyperfine tensors determined by the simulation of the X- and Q-band single-crystal and solution EPR spectra are as follows: $g_x = 1.9887$, $g_y = 1.9957$, $g_z = 1.9775$, and hyperfine coupling constants are $A^{III}{}_x = |171|$ G, $A^{III}{}_y = |176|$ G, $A^{III}{}_z = |129|$ G, $A^{IV}{}_x = |77|$ G, $A^{IV}{}_y = |74|$ G, $A^{IV}{}_z = |80|$ G.

[*]jyano@lbl.gov; vkyachandra@lbl.gov.

Supporting Information Available: The k^3-weighted polarized Mn EXAFS spectra (Figure 1S) and the Fourier Transforms of EXAFS (Figure 2S). This material is available free of charge via the Internet at http://pubs.acs.org.

Introduction

Manganese clusters with μ-oxo bridged structures are known to play an important role at the active site in several metalloenzymes, such as catalase and the oxygen-evolving complex (OEC) of photosystem (PS) II.[1–5] The OEC contains a cluster of 4 manganese atoms that catalyzes the oxidation of water to dioxygen. This reaction is a stepwise process wherein 4 photons absorbed sequentially by the reaction center power the advance of the OEC through the S-state intermediates ($S_0 - S_4$ states). The first direct spectroscopic evidence for the association of Mn with the S-state intermediates emerged from the discovery of a multiline EPR signal (MLS) centered at $g = 2$ with hyperfine structure characteristic of ^{55}Mn ($I = 5/2$).[6] On the basis of its flash-number dependence, the MLS was associated with the S_2 state. The similarity of this signal to the EPR spectrum of a Mn_2(III,IV) complex with $S = 1/2$ ground state led to a proposal for the oxidation state of the Mn cluster. At present, the generally accepted interpretation of the S_2 state MLS is that it arises from an $S = 1/2$ antiferromagnetically exchange-coupled high spin Mn_4(III,IV_3) species.[5,7] A similar MLS EPR signal has been discovered from the S_0 state.[8–10]

Multinuclear, especially binuclear, Mn model complexes have been extensively studied by several groups[11–16] in the hope that a clear understanding of simple model systems would shed light on the much more complicated natural system, which remains poorly understood.[17–19] The EPR MLS from the OEC contains key information about electronic structures, oxidation states, and ligand environment of the Mn cluster. A variety of di-μ-oxo-bridged Mn_2(III,IV) compounds with a distinct 16 hyperfine line EPR signal, similar to that of the OEC in the S_2 state, have been reported. The origin of this MLS was first explained by Cooper et al.[20] as an antiferromagnetically coupled ^{55}Mn ($I = 5/2$) binuclear mixed-valence complex of Mn(III) ($S = 2$) and Mn(IV) ($S = 3/2$) with $S = 1/2$ ground state. Using the spin-coupled model, it was determined that the intrinsic hyperfine constant of Mn(III) is twice as large as that of Mn(IV) for such a system, leading to the characteristic 16 lines assuming isotropic g and ^{55}Mn hyperfine tensors of approximately |167| G for Mn(III) and |79| G for Mn(IV). However, the above explanation ignored the anisotropic characteristics of the experimental spectra, and the clear discrepancy between the experimental and simulated spectra of Mn(III)Mn(IV) complexes remained unexplained. Thus, it was difficult to elaborate further the electronic structures of these molecules. Recent studies, however, have attempted to simulate the EPR signals of the di-μ-oxo-bridged Mn model systems by considering the anisotropic characteristics of the multiline signals by utilizing EPR at different fields and related techniques such as ESEEM and ENDOR.[11,13–16,21]

In this study, we have utilized single-crystal EPR spectroscopy at two microwave frequencies, X (9 GHz) and Q (34 GHz) bands, to obtain a very precise anisotropic data set for a Mn(III)Mn(IV) complex directly from EPR spectra collected with the external magnetic field aligned along a specific crystal axis. Multiline EPR signals contain contributions from g anisotropy and hyperfine anisotropy. A combination of X- and Q-band measurements allows us to emphasize the contribution of anisotropic characteristics of g-values to the spectra, since the effect is enhanced at the higher magnetic fields, while the hyperfine interactions are not affected. In addition, the EPR study using single crystals provides a direct method of resolving and orientationally selecting EPR features that are unresolved in the spectra of unoriented solution samples. We measured the X-ray diffraction and polarized X-ray absorption spectra (XAS) using the same crystals. The X-ray diffraction and the extended X-ray absorption fine structure (EXAFS) region of XAS together with single-crystal EPR spectra allowed us to relate the principal axes of molecules directly to the g and hyperfine tensors along those axes.

The complex used in the present study is a binuclear di-μ-oxo-bridged Mn compound with phenanthroline terminal ligands, $[Mn_2(III,IV)O_2(phen)_4](PF_6)_3{\cdot}CH_3CN$. The synthesis and the crystal structure of this complex has been reported by Stebler et al.[22] We chose this crystal for our study because the four molecules in the crystal unit cell line-up in nearly the same orientation; this enormously simplifies making a relation between the crystal and molecular axes, and facilitates determining the hyperfine anisotropy and *g* anisotropy of a molecule. In single-crystal studies of pure complexes, high magnetic concentrations lead to line-broadening via spin–spin interactions, and this effect often creates a limitation for orientational resolution. In this complex, however, the unique molecular arrangements seemed to avoid significant line-broadening and this made it possible to obtain the unique set of anisotropic *g* values and hyperfine tensors. These parameters were related to the molecular axes by the results from single-crystal EXAFS measurements and X-ray diffraction. On the basis of these results, we discuss the relationship of EPR features and the electronic environment of the Mn(III)Mn(IV) system. This is the first such study, to our knowledge, of binuclear Mn complexes that has utilized single-crystal EPR studies at different fields to assign anisotropic *g* and hyperfine parameters.

Experimental Section

Single-Crystal Samples—Three binuclear di-μ-oxo-bridged Mn_2(III,IV) compounds with phenanthroline or bipyridine terminal ligands, and PF_6^- or ClO_4^- counterions, were used in this study. They are as follows: $[Mn_2(III,IV)O_2(phen)_4](PF_6)_3{\cdot}CH_3CN$, $[Mn_2(III,IV)O_2(phen)_4](ClO_4)_3{\cdot}H_2O$, and $[Mn_2(III,IV)O_2(bipy)_4](ClO_4)_3{\cdot}H_2O$. These crystals have a diamond-shaped plate morphology. The solution samples were prepared by dissolving the crystals in acetonitrile solvent.

EPR Spectra Measurements—Single crystal and solution EPR spectra were collected at 9.25 GHz (X-band) and 34.5 GHz (Q-band) frequencies at 9 K. X-band EPR spectra were collected using a Varian E-109 spectrometer equipped with an E-102 microwave bridge. Temperature was controlled by an Air Products Helitran liquid helium cryostat. Q-band EPR spectra were collected using a Bruker EPR spectrometer (EMX 10/12 with ER5106QT Flexline resonator). Temperature was maintained using a liquid helium cryostat (Oxford Instruments). Both X- and Q-band measurements were taken with 100 kHz magnetic field modulation. The microwave frequency was calibrated using a standard sample of TEMPO (Aldrich, 30 μM, 50 v/v% glycerol solution). The single-crystal sample was rotated in the liquid He dewar/EPR cavity using a home-built goniometer.

EPR Spectra Analysis—In the Mn(III)Mn(IV) system, which has two hyperfine centers, the effective EPR spin Hamiltonian with the total spin of S = 1/2 is written as

$$H=\beta_e gBS+SA^{\mathrm{III}}I+SA^{\mathrm{IV}}I \quad (1)$$

where A^{III} and A^{IV} are the hyperfine coupling tensors for Mn(III) and Mn(IV), *I* is the nuclear spin (*I* = 5/2 for ^{55}Mn), *B* is the magnetic field, β_e is the Bohr magneton, *g* is the effective g tensor, and *S* is the total electron spin. For a Mn(III)Mn(IV) system with antiferromagnetically coupled S^{III} (Mn(III)) = 2 and S^{IV} (Mn(IV)) = 3/2 states that generate a *S* = 1/2 ground state, the g tensor from the coupled Mn(III) and Mn(IV) ions is[23–25]

$$g=2g^{\mathrm{III}}-g^{\mathrm{IV}}-\frac{2}{5J}\left(g^{\mathrm{III}}-g^{\mathrm{IV}}\right)\left(7D^{\mathrm{III}}+2D^{\mathrm{IV}}\right) \quad (2)$$

where g^{III} and g^{IV} are the *g* tensors of monomeric Mn(III) and Mn(IV) ions, *J* is the isotropic exchange coupling constant ($H = -2JS^{\mathrm{III}}S^{\mathrm{IV}}$), and D^{III} and D^{IV} are the zero-field

splitting tensors of the monomeric Mn^{III} and Mn^{IV} ions.[25] In the same manner, the magnetic hyperfine tensors of the coupled two nuclei, A^{III} and A^{IV}, can be written as

$$A^{\mathrm{III}}=2a^{\mathrm{III}}+\frac{2}{5J}\left(7D^{\mathrm{III}}+2D^{\mathrm{IV}}\right)a^{\mathrm{III}} \quad (3)$$

$$A^{\mathrm{IV}}=-a^{\mathrm{IV}}-\frac{2}{5J}\left(7D^{\mathrm{III}}+2D^{\mathrm{IV}}\right)a^{\mathrm{IV}} \quad (4)$$

where a^{III} and a^{IV} are hyperfine tensors of the monomeric Mn(III) and Mn(IV) ions.

For a rhombic system, eq 1 is written as

$$H=\beta_e B\sum_{i=x,y,z} g_i S_i+\sum_{i=x,y,z} S_i {A_i}^{\mathrm{III}} I_i+\sum_{i=x,y,z} S_i {A_i}^{\mathrm{IV}} I_i \quad (5)$$

EPR solution spectra were simulated by the programs developed by White and Belford[26,27] for the total spin of $S = 1/2$ systems and modified by our group. The program includes second-order hyperfine interaction up to the second nuclei. The two isolated spin systems were added using the vector projection model for the exchange-coupled system.

For the simulation of single-crystal EPR spectra, we used a modified version of the programs to calculate the EPR spectra at specified angles of the magnetic field with respect to the *g* and hyperfine tensors. Slightly different microwave frequencies for individual spectra lead to small shifts of the spectra on the magnetic field axis relative to each other. Therefore, the simulation was done using the precise microwave frequencies of the individual spectra.

X-ray Diffraction Measurements—Indexing of the crystals was carried out by standard X-ray diffraction methods (Rigaku/MSC). Crystals were mounted on a 2-circle goniometer, and the diffraction data were collected using a Mar345 imaging plate detector (MAR USA Inc.). The data collection was carried out at room temperature.

X-ray Absorption Measurements—X-ray absorption spectra were taken at the Stanford Synchrotron Radiation Laboratory (SSRL) on beamline 9–3 at an electron energy of 3.0 GeV with an average current of 70–90 mA. The radiation was monochromatized by a Si(220) double-crystal monochromator which was detuned at 6600 eV to 50% of maximal flux to attenuate the X-ray 2nd harmonic. Intensity of the incident X-ray was monitored by an N_2-filled ion chamber (I_0) in front of the sample. Data were taken as fluorescence excitation spectra using a germanium 30-element energy-resolving detector (Canberra Electronics). Energy was calibrated by the preedge peak of $KMnO_4$ (6543.3 eV), which was placed between two N_2-filled ionization chambers after the sample. The sample crystal was mounted on a two-circle goniometer, and spectra were taken at several orientations by rotating the crystal relative to the incident polarized X-ray radiation.

A combination of XANES and EXAFS spectra was collected from 6400 to 7100 eV at room temperature; 3 eV/point from 6400 to 6535 eV, 0.2 eV/point from 6535 to 6576 eV, and 0.05 $Å^{-1}$/point in *k*-space from 2.07 to 12.0 $Å^{-1}$ (6576 eV to 7100 eV). In the *k*-space region, collection time was weighted using a cubic function from a minimum of 1 s per point at low *k* values to a maximum of 15 s per point at high *k* values. The EXAFS analysis was performed following methods described in detail previously.[28]

Coordinate System and the Crystal Structure of Mn_2(III,IV) Di-μ-oxo Bridged Phenanthroline Complex—An *x*,*y*-rotated coordinate system was used for the definition of *g* and hyperfine tensors of $[Mn_2(III,IV)O_2(phen)_4]$ according to Gamelin et al. (Figure 1).[29] The site symmetry of the Mn_2O_2 moiety is approximately C_{2V}, and the *z*-axis is defined to be perpendicular to the di-μ-oxo-plane. The *x*- and *y*-axes are defined as two orthogonal axes in the di-μ-oxo-plane; the *x*-axis is parallel to the Mn–Mn vector, while the *y*-axis is perpendicular to it.

The crystal structure of $[Mn_2(III,IV)O_2(phen)_4](PF_6)_3{\cdot}CH_3CN$ has been reported.[22] It crystallizes in the orthorhombic, space group *P*bcn with *a* = 9.891 (3) Å, *b* = 22.690 (9) Å, *c* = 22.858 (8) Å, *Z* = 4. Figure 2 shows the projections of molecules in the crystal unit cell. The Mn–oxo–Mn planes are in the *ac*-plane and the Mn–Mn vectors are nearly parallel to the *c*-axis of unit cell. Table 1 specifies the relation between the molecular axes and the crystallographic axes more precisely. The *z*-axis of the molecule is parallel to the *b*-axis and perpendicular to the *a*- and *c*-axes. As can be seen in Figure 2, the Mn–Mn vector of each molecule is approximately 7° from the *c*-axis in the *ac*-plane, and the neighboring molecules (indicated as Molecule I and II in Table 1) are related by the 2-fold rotation axis symmetry. Thus, the *a*- and *c*-axes are nearly parallel to the *y*- and *x*-axes of molecules with approximately 7° of deviation.

Results

Determination of the Orientation of the Single Crystal

The orientation of a crystal was determined using both polarized EXAFS and X-ray diffraction. X-ray diffraction was used to screen the crystals and index them. The crystals were mounted on small Mylar strips for EPR measurements and, after the EPR measurements, the same crystals were used for polarized EXAFS measurement to obtain the direction of the Mn–Mn vector and Mn_2O_2 plane to a high degree of accuracy.

The single crystal of $[Mn_2(III,IV)O_2(phen)_4](PF_6)_3{\cdot}CH_3CN$ was mounted on the goniometer such that the crystal long axis was parallel to the X-ray **e**-vector and the crystal face was perpendicular to the incoming X-ray beam ($\varphi_{crystal}$ = 0°, $\chi_{crystal}$ = 0°) (see Supporting Information). Then polarized XAS spectra were taken by rotating the crystal about the φ- and χ-axes. The unique set of polarized spectra were obtained at the three extreme orientations, ($\varphi_{crystal}$, $\chi_{crystal}$) = (0°, 0°), (0°, 90°), and (90°, 0°) which are parallel to the crystal *c*-, *a*-, and *b*-axes, respectively. A comparison of the crystal structure and the polarization characteristics of Mn EXAFS explains well the relation between the orientation of crystallographic axes and crystal morphology. The *c*-axis, which is parallel to the Mn–Mn vector, coincides with the direction of the long axis of the crystal, and the *b*-axis is perpendicular to the crystal face. The *a*-axis is parallel to the short axis of the crystal. Thus, the molecular geometry and distances obtained from polarized EXAFS coincide well with the crystallographic data. The orientation of the crystallographic axes was also obtained by X-ray diffraction measurement, which confirmed the molecular orientation that emerged from polarized EXAFS.

This methodology allowed us to obtain independent data on the orientation of the same single crystal, in the same sample holder, as was used for EPR measurements after the XRD measurements. These studies provide the underpinning for the assignment of the anisotropic EPR parameters and their correlation to the molecular axes of the complex.

Single-Crystal X- and Q-Band EPR Spectra

Using the EXAFS and XRD results as an indicator of crystal orientation, the EPR spectra in the crystallographic *ab*- and *bc*-planes were collected by rotating the crystal around the *c*- and *a*-axes, respectively (Figure 3). Figure 3a shows the X-band spectra in the *ab*-plane. A crystal was mounted in the EPR cavity such that the magnetic field (B) is parallel to the crystallographic *a*-axis (0° orientation). Then the crystal was rotated around the *c*-axis by 10° steps to 170°. At 90°, the magnetic field coincided with the direction of the *b*-axis of the crystal. In the same manner, single-crystal spectra were taken in the *bc*-plane. In Figure 3b, the magnetic field is parallel to the *c*-axis at the 0° setting and parallel to the *b*-axis at 90°. The spectra show clear hyperfine splitting in all orientations and exhibit a 180° periodicity, as expected from the symmetry of the crystal. Depending on the orientation of the crystal, both the number of hyperfine components and the center of the hyperfine signal change, showing the strong anisotropic characteristics in both *ab*- and *bc*-planes. The spectra along the *a*-, *b*-, and *c*-axes, identified in red in Figure 3a,b, exhibit a total width of ~1350 G, ~1170 G, and ~1290 G, respectively.

We also measured the Q-band EPR spectra, using the same crystal and following a similar protocol; the Q-band spectra in the *ab*- and *bc*-planes are shown in Figure 3c,d. The total width of the spectra is similar to that observed for the X-band data. However, the relative center of the spectrum among three extreme orientations is clearly different, indicating the presence of significant g anisotropy.

These unique spectral features along the *a*-, *b*-, and *c*-axes show the rhombic symmetry of g-values and ^{55}Mn hyperfine couplings. In the following section, we describe the simulation of these three spectra by taking into account the molecular arrangement in the crystal.

Simulation of Single-Crystal EPR Spectra

The molecular site symmetry of the di-μ-oxo bridged Mn_2O_2 planar unit is approximately C_{2v}. Therefore, this symmetry was used for the definition of the molecular orientation for the simulation of the single-crystal EPR spectra (see Figure 1).[30] The angle θ defines the tilt angle of the magnetic field (B) from the *z*-axis, and φ defines the angle of B in the *xy*-plane. The noncoincident angle, R, between *g* and hyperfine tensor axes was assumed to be zero in the initial simulation. The spectrum parallel to the *b*-axis of the crystal was used for the determination of the *z*-components of *g* and hyperfine parameters, since *b*//*z* ((θ, φ) = (0°, 0°)). For the determination of *x* and *y* components, the spectra parallel to the *c*- and *a*-axes were used, respectively. As indicated in Table 1, the *x*- and *y*-axes of the neighboring molecules have a small orientational deviation; those axes are approximately 7° from the crystallographic axes and directed away from each other. Incorporating these deviations, the θ and φ angles for the simulation of the polarized spectrum along each crystal-lographic axis were set as (θ, φ)) (90°, 83°) for *a*, (0°, 0°) for *b*, and (90°, 7°) for the *c*-axis. The angle dependence of the *g* value is obtained by the following equation.[30-32]

$$g(\theta,\phi)=\left(g_x{}^2l^2+g_y{}^2m^2+g_z{}^2n^2\right)^{1/2} \quad (6)$$

with the direction cosines, $l = \sin\theta\cos\varphi$, $m = \sin\theta\sin\varphi$, and $n = \cos\theta$.

The angle dependence of the ^{55}Mn hyperfine coupling, $\mathbf{A}(\theta,\varphi)$, is given by

$$g(\theta,\phi)^2A(\theta,\phi)^2=(lg_xA_{xx}+mg_yA_{yx}+ng_zA_{zx})^2+(lg_xA_{xy}+mg_yA_{yy}+ng_zA_{zy})^2+(lg_xA_{xz}+mg_yA_{yz}+ng_zA_{zz})^2 \quad (7)$$

In the case where the hyperfine tensor axes coincide with the *g* tensor axes, eq 7 can be simplified as (see Figure 1)

$$g(\theta,\phi)^2 A(\theta,\phi)^2 = (l g_x A_x)^2 + (m g_y A_y)^2 + (m g_z A_z)^2 \quad (8)$$

The approximate *g* values were obtained from the center of the hyperfine lines along each crystallographic axis, first with X-band spectra and then more precisely with Q-band spectra. A set of *g* values thus obtained was used for fitting the hyperfine parameters, initially assuming a constant Gaussian line width. Fitting was completed when a consistent set of *g* value and hyperfine parameters for both frequency bands was found that could not be improved further. The best fit was obtained with the Gaussian line width (half width at half-maximum for the absorption spectrum) of 69 G along the *c*-axis, 45 G along the *a*-axis, and 57 G along the *b*-axis, independent of the frequency of the microwaves. In Figure 4, the solid lines show the experimental spectra, and the dotted lines show the results of the single-crystal EPR simulation. The final values obtained from these spectra were, g_x = 1.9860 (±0.0010), g_y = 1.9935 (±0.0010), g_z = 1.9740 (±0.0008), $A^{III}{}_x$ = |170 (±2)|, $A^{III}{}_y$ = |176 (±2)|, $A^{III}{}_z$ = |129 (±2)|, $A^{IV}{}_x$ = |76(±2)|, $A^{IV}{}_y$ = |75 (±2)|, $A^{IV}{}_z$ = |79 (± 2)| G. We also tried to include the effect of the noncoincident angle α between the g and the hyperfine tensors (Figure 1). The quality of simulation improved at an α = 5°, but the effect was not significant.

The relatively large line width is due to the high spin concentration in the single crystals leading to a low resolution of the anisotropic parameters determined above. Therefore, the final determination of the *g* and hyperfine tensors was carried out by applying those parameters to the simulation of the solution spectra.

Simulation of Solution Spectra

Solution spectra were taken by dissolving crystals of $[Mn_2(III,IV)O_2(phen)_4](PF_6)_3{\cdot}CH_3CN$ in acetonitrile. The spectra showed a typical 16 line EPR spectrum at X- and Q-bands, as reported in the literature from Mn(III)Mn(IV) exchange-coupled complexes (Figure 5).[20] Using the *g* values and hyperfine constants obtained from the simulation of single-crystal EPR spectra as starting parameters, we carried out the fitting of solution spectra at both frequencies. The line width of hyperfine coupling was kept constant at 15 G, and we kept the noncoincident angle at 0°. The final set of *g* values and hyperfine constants obtained are listed in Table 2 and the simulated spectra are plotted as dotted lines in Figure 5. The obtained data set yielded consistent results in simulating the solution spectra at both X- and Q-band frequencies. The single-crystal spectra were reasonably reproduced using these values at both frequencies.

Discussion

In this study, the orientation of the g and hyperfine tensor axes of $[Mn_2(III,IV)O_2(phen)_4](PF_6)_3{\cdot}CH_3CN$ complex with respect to the molecular structure was obtained directly from the single-crystal EPR spectra. We obtained a rhombic g and hyperfine tensor system with g_x = 1.9887, g_y = 1.9957, g_z = 1.9775, $A^{III}{}_x$ = |171| G, $A^{III}{}_y$ = |176| G, $A^{III}{}_z$ = |129| G, $A^{IV}{}_x$ = |77| G, $A^{IV}{}_y$ = |74| G, $A^{IV}{}_z$ = |80| G.

The hallmark of EPR spectrum from exchange-coupled oxo-bridged Mn_2(III,IV) clusters was the observation of 16 hyperfine lines assigned to a coupling of the Mn(III) and Mn(IV) nuclei. The presence of 16 hyperfine lines instead of the 36 expected lines (with isotropic *g* and hyperfine values) was attributed to overlap of the hyperfine lines caused by the two-to-one ratio of the A^{III} to A^{IV} hyperfine values. Even in studies at Q-band where the presence of anisotropy should be apparent, the solution EPR spectrum still exhibited only 16 lines. The single-crystal EPR spectra shown in Figure 3a–d clearly demonstrate the presence of both g and hyperfine anisotropy; therefore, the traditional explanation for the 16 line

spectrum is too simplistic. In the single crystal spectra, the number of lines ranges from 8 to 16 as a function of the orientation. It is because (1) the relatively large line width of single-crystal EPR spectra makes some lines unresolved, (2) the two-to-one ratio of A^{III} to A^{IV} does not hold in all directions, and (3) the number of lines resolved in a specific orientation depends on the anisotropic line width. In the following part, we discuss the origin of anisotropic *g* and ^{55}Mn hyperfine parameters and line width by comparing them to the parameters of mononuclear Mn(III) and Mn(IV) ions.

g-Values

The present EPR study of single crystals shows that the rhombic *g* values are in the order $g_z < g_x < g_y$. The lowest *g* value is along the direction of the molecular *z*-axis, which is perpendicular to the di-μ-oxo plane. The g_x value is along the Mn–Mn direction, and it is smaller than g_y, which is along the axis that bisects the Mn–O–Mn. The EPR spectra and anisotropic g and A values derived from these spectra clearly indicate the valence-trapped nature of the mixed valence complex. Hence, reviewing the g-values from Mn(III) and Mn(IV) monomers is useful for understanding the origins of *g* and *A* anisotropy in this complex.

In a typical Mn(III) monomer[33] with d^4 configuration ($^3t_{2g}{}^1e_g$), a single unpaired electron occupies the σ antibonding d_z^2 orbital. This leads to the distorted octahedral environment with Jahn–Teller distortion along the d_z^2 direction,[34] with a $^5B_1$ ground state.[33] The deviation of the *g* values along the tetragonally distorted axis and in the equatorial direction for such a ground-state configuration can be described by the equations described in the footnote.[35] These show that the $g_{\parallel}$ along the d_z^2 direction will be smaller compared to $g_{\perp}$ in the *x* and *y* direction. No differences have been observed in the *g*-values in the equatorial directions (*x* and *y*) in Mn(III)(dbm)$_3$ and Mn(III) in rutile in which the six oxo ligands are structurally equivalent in the *x*, *y*, *z* directions.[33,36] On the other hand, rhombic *g* values have been reported for the [(terpy)Mn^{III}(N$_3$)$_3$], (terpy, 2,2′:6′2″-terpyridine) complex where the six N ligands are structurally nonequivalent.[37]

For the Mn(IV) monomer with a d^3 configuration ($^3t_{2g}$), the anisotropy in the *g* values is usually smaller compared to the Mn(III) ion due to the symmetric electronic configuration.[38–40] The deviation of the *g* value is in the vicinity of 0.004 for Mn(IV) depending on the ligand environment, while in the vicinity of ~0.02 for Mn(III).

In the mixed valence system of [Mn$_2$(III,IV)O$_2$(phen)$_4$](PF$_6$)$_3$·CH$_3$CN, the deviation of the *g*-value is 0.018, with the smallest *g* value along the molecular *z*-direction (g_z). Although the g tensor derives from both Mn(III) and Mn(IV) centers, the present result clearly shows that most of the g anisotropy of the Mn(III)Mn(IV) system arises from the Mn(III) center. The crystallographic data of Mn(III)Mn(IV) complexes usually exhibit a longer Mn–N$_{ax}$ bond (molecular *z*-direction) length at the Mn(III) site, indicating the presence of distinct Mn(III) and Mn(IV) sites in the Mn(III)Mn(IV) complexes.[41–47] Just as in the case of the Mn(III) monomer, the unpaired electron occupies the d_z^2 orbital of the Mn(III) site in the Mn(III)-Mn(IV) di-μ-oxo complex.[29] By assuming a $^5B_1$ ground state,[13] the rhombic *g* values along each of the molecular axes can be described by the following equations[35]

$$g_z = g_e - \frac{8\lambda}{\Delta E\,(z^2 \rightarrow xy)} \quad (9)$$

$$g_x = g_e - \frac{2\lambda}{\Delta E\,(xz \rightarrow xy)} \quad (10)$$

$$g_y = g_e - \frac{2\lambda}{\Delta E\,(yz \rightarrow xy)} \quad (11)$$

where ΔE is the energy difference between the ground state and the excited state and d_{xy} is the excited state in the present case.[29] It is clear from eqs 9–11 that g_z will be the lowest value, as is observed experimentally. In the Mn(III)Mn(IV) complexes, *x* and *y* directions are structurally nonequivalent (Figure 1). In addition, the bonding interactions between the metal *d*-orbitals and oxygen *p*-orbitals are different in the *x* and *y* directions. The crystallographic data show that the oxo-Mn-oxo angle is 84°, whereas Mn–oxo–Mn angle is 96°. The acute angle of oxo-Mn-oxo indicates stronger interaction along the *x*-direction. Therefore, the energy level of $d_{xz} > d_{yz}$ and, as a consequence, $g_x < g_y$ according to eqs 10 and 11. Our experimental data are consistent with this theoretical observation.

Hyperfine Coupling

In the present study we have obtained rhombic hyperfine tensors, $A^{III}{}_x = -171$, $A^{III}{}_y = -176$, $A^{III}{}_z = -129$, $A^{IV}{}_x = 77$, $A^{IV}{}_y = 74$, $A^{IV}{}_z = 80$ G, with the anisotropy of $\Delta A^{III} = 47$ G and $\Delta A^{IV} = 76$ G. The sign of these hyperfine coupling constants has been explained in the literature.[20] The result shows the strong anisotropic character in Mn(III), but less in Mn(IV). In the Mn(IV) d^3 monomer,[39] the magnetic hyperfine tensors are nearly isotropic due to the symmetric electronic configuration ($^3t_{2g}$). Some exceptions have been observed in strongly perturbed octahedral environments.[40] On the other hand, large hyperfine anisotropy has been observed in Mn(III) d^4 monomers ($^3t_{2g}{}^1e_g$).[31,33,48] In addition, the zero-field splitting of the Mn(IV) ions is smaller ($|D^{IV}| < 1$ cm^{-1})[39,40] than the value of Mn(III) ions ($|D^{III}| \approx 4$ cm^{-1}).[33,36,37] In the Mn(III)Mn(IV) mixed valence system, the anisotropy transfer from Mn(III) to Mn(IV) through zero-field splitting perturbation arises from the second term of eqs 3 and 4. We expect from the above observations that the hyperfine anisotropy of Mn(III) can be basically explained by the intrinsic Mn(III) hyperfine anisotropy, while the major source of the Mn(IV) hyperfine anisotropy arises from the transferred zero-field splitting perturbation from Mn(III).[11,15,25]

In the following section we compare our experimental values with the calculated values using the intrinsic values reported for Mn(III) and Mn(IV) ions. The intrinsic hyperfine tensors for the monomeric Mn(III) ions in TiO_2 are from Gerritsen and Sabisky[33] who reported values of $A_{x,y} = 88.8$ G and $A_z = 56.5$ G with $D = -3.4 \pm 0.1$ cm^{-1} and $E = 0.116 \pm 0.001$ cm^{-1}. For Mn(IV) ion in TiO_2, From et al.[40] obtained values of $A_x = 77.7 \pm 0.5$ G, $A_y = 75.4 \pm 0.5$ G, and $A_z = 80.6 \pm 0.5$ G with $D = 0.8818 \pm 0.003$ cm^{-1} and $E = 0.2635 \pm 0.003$ cm^{-1}. When these two isolated spin systems are combined using the vector projection model for exchange-coupled systems, the expected hyperfine terms of Mn(III)Mn(IV) complexes are $A^{III}{}_{x,y} = |172|$ G, $A^{III}{}_z = |110|$ G, $A^{IV}{}_x = |72|$ G, $A^{IV}{}_y = |69|$ G, $A^{IV}{}_z = |74|$ G, with anisotropy of $\Delta A^{III} = 62$ G and $\Delta A^{IV} = 5$ G from eqs 3 and 4, using $J = -148$ cm^{-1}, $D^{III} = -3.4$ cm^{-1} and $D^{IV} = 0.8818$ cm^{-1}.

The experimental values are in the range of the theoretically expected values, except for the smaller hyperfine anisotropy for the Mn(III) site. The hyperfine anisotropy of the Mn(IV) site is significantly smaller than that of the Mn(III) site, which is consistent with the trend in the Mn(IV) monomers ($A^{IV}{}_y < A^{IV}{}_x < A^{IV}{}_z$). For the Mn(III) center, the smallest hyperfine coupling along the *z*-direction is consistent with the calculated hyperfine coupling value of the Mn(III) monomer with the $^5B_1$ ground state.[48] The smaller value along the *x*-axis ($A^{III}{}_x$) compared with that along the *y*-axis ($A^{III}{}_y$) could be the consequence of the rhombic electronic environment at the Mn(III) site due to the nonequivalent electron density in the *x* and *y* directions, as was mentioned in the previous section. We do not have a definitive explanation for a smaller hyperfine anisotropy for the Mn(III) site compared to the

calculated values. However, possible reasons are as follows; (1) In the Mn(III)Mn(IV) mixed valence system, the electron is not completely localized, and the electron density can be transferred from the d_z^2 orbital on one center (Mn(III)) to the $d_{x^2-y^2}$ orbital on the other (Mn(IV)) in C_2 symmetry.[49,50] This may modify hyperfine anisotropy of the two Mn centers, mostly decreasing the anisotropic effect at the Mn(III) site. (2) The hyperfine tensors (A^{III} and A^{IV}) and the zero-field splitting tensors (D^{III} and D^{IV}) of the intrinsic Mn(III) and Mn(IV) ions we used for the calculations are both from the six O-ligand complexes, rather than from mixed N and O ligand complexes. We know of no appropriate Mn monomers which have a mixed ligand environment; therefore, the present calculation does not include this effect.

Interestingly, the crystallographic data of $[Mn_2(III,IV)O_2(phen)_4](PF_6)_3{\cdot}CH_3CN$ do not show the difference between Mn(III) and Mn(IV), unlike other reported crystal structures of Mn(III)Mn(IV) di-μ-oxo complexes.[41–44] This is probably due to the transposition of Mn(III)–Mn(IV) and Mn(IV)–Mn(III) units in the crystal as Stebler et al. mentioned.[22] This structural disorder is the possible reason for the small difference between the averaged distances of $Mn–N_{equatorial}$ and $Mn–N_{axial}$ ($\Delta\{(Mn–N_{equatorial})–(Mn–N_{axial})\} \approx 0.02$ Å); in other reported crystal structures of Mn(III)Mn(IV) system, the difference is in the range of 0.05–0.1 Å. In fact, the evidence of the trapped Mn(III) and Mn(IV) valences in $[Mn_2(III,IV)O_2(phen)_4](PF_6)_3{\cdot}CH_3CN$ is clear in the present EPR spectra; two distinct hyperfine couplings of Mn(III) and Mn(IV) are observed in the *x*, *y*, and *z* directions, which we do not expect from the system where the spin is completely delocalized on two Mn centers.

Line Width

In general, hyperfine splitting is not observed in single crystals of Mn(III)Mn(IV) complexes due to the broadening of the individual absorption curves caused by the large spin–spin interaction. In the single-crystal spectra of $[Mn_2(III,IV)O_2(bipy)_4](ClO_4)_3{\cdot}H_2O$ and $[Mn_2(III,IV)O_2(phen)_4](ClO_4)_3{\cdot}H_2O$, for example, only a single broad peak (~1350 G peak-to-peak width of the 1st derivative) was observed at any crystal orientation in the X-band measurement. On the contrary, we have observed clear hyperfine splitting and, therefore, an unique angle dependence of hyperfine couplings from a single crystal of the $[Mn_2(III,IV)O_2(phen)_4](PF_6)_3{\cdot}CH_3CN$ complex.

In the magnetically concentrated systems, the line width is the result of (A) magnetic dipole–dipole interaction and (B) the exchange interaction between the neighboring spins.[51–58] The former factor causes line broadening, while the latter narrows the line width. For the $[Mn_2(III,IV)O_2(phen)_4](PF_6)_3{\cdot}CH_3CN$ complex, we have not observed any significant difference of the line width at both X- and Q-band measurements, as seen by the clear hyperfine and g anisotropy at both frequencies. We can therefore conclude that the hyperfine interaction and the g anisotropy are much larger than the effect of the intermolecular exchange coupling in our system.

The above fact implies that the significant difference of the line broadening among the $[Mn_2(III,IV)O_2(phen)_4](PF_6)_3{\cdot}CH_3CN$, $[Mn_2(III,IV)O_2(bipy)_4](ClO_4)_3{\cdot}H_2O$, and $[Mn_2(III,IV)O_2(phen)_4](ClO_4)_3{\cdot}H_2O$ crystals can be explained mainly by the dipole–dipole coupling caused by the differences of (1) the neighboring spin–spin distances, (2) the angle between the static magnetic field and the vector connecting the two interacting spins, and (3) the position and the kind of counterions and solvent molecules.

As far as the center-to-center distances of molecules are concerned, we have not observed a significant difference between $[Mn_2(III,IV)O_2(phen)_4](PF_6)_3{\cdot}CH_3CN$ and $[Mn_2(III,IV)O_2(bipy)_4](ClO_4)_3{\cdot}H_2O$ crystals (Figure 6). The former crystal has center-to-

center distances of the neighboring molecules between 9.9 and 18.8 Å. The shortest Mn–Mn distance is 9.9 Å. For the latter crystal, which has the space group of $P2_1/c$, the center-to-center distances are between 9.8 and 14.5 Å. The shortest Mn–Mn distance is 9.7 Å.[58]

However, the molecular orientations are significantly different in $[Mn_2(III,IV)O_2(phen)_4](PF_6)_3{\cdot}CH_3CN$ and $[Mn_2(III,IV)O_2(bipy)_4](ClO_4)_3{\cdot}H_2O$ crystals. By considering the center-to-center distances of molecules and with these orientations, we calculated the line broadening effect in the following manner. The dipole interaction from a neighboring identical dipole μ can be expressed as $\mu(1\text{-}3\cos^2\theta_{ij})/r_{ij}^3$, where θ_{ij} is the angle between the static magnetic field and the vector connecting the center of two interacting dipoles (i,j) and r_{ij} is the distance between dipoles. The approximate line broadening effect of the dipolar-dipolar interaction can be evaluated by the second moment

$$\left(\Delta H^2{}_{\mathrm{ave}}\right) = \frac{3}{4} g^2 \beta^2 S\,(S+1) \sum_i \left(1 - 3\cos^2\theta_{ij}\right)^2 r_{ij}{}^{-6} \quad (12)$$

By considering the neighboring molecules closer than 15 Å, we have obtained $\Delta H^2_{ave} \approx$ 23–28 G for $[Mn_2(III,IV)O_2(phen)_4](PF_6)_3{\cdot}CH_3CN$ and 25–43 G for $[Mn_2(III,IV)O_2(bipy)_4](ClO_4)_3{\cdot}H_2O$ crystals, depending on the crystal orientation. This is suggestive that the smaller dipolar-dipolar interaction in $[Mn_2(III,IV)O_2(phen)_4](PF_6)_3{\cdot}CH_3CN$ due to the simple molecular arrangement is one of the main reasons to prevent the severe line broadening, which would otherwise veil hyperfine splitting in a magnetically concentrated system. As mentioned before, however, the best fit of the single-crystal EPR spectra of $[Mn_2(III,IV)O_2(phen)_4](PF_6)_3{\cdot}CH_3CN$ was obtained with a Gaussian line width of 69 G for c, 45 G for a, and 57 G for the b direction at both X- and Q-band frequencies; the numbers are much larger than the calculated line width for both $[Mn_2(III,IV)O_2(phen)_4](PF_6)_3{\cdot}CH_3CN$ and $[Mn_2(III,IV)O_2(bipy)_4](ClO_4)_3{\cdot}H_2O$.

Concerning the third point, the type of counterions and solvent molecules modifies the space group and the unit cell parameters, and therefore the molecular arrangements.[59,60] The counterions and solvent molecules may also weakly coordinate with metal ions, modifying the exchange interaction. Felthouse et al. have discussed the effect of counterions for $[Cu_2(dien)_2(C_2O_4)](X)_2$ (counterion X as BPh_4, PF_6, or ClO_4)[60] When the counterions are weakly coordinated, they mediate intermolecular exchange interaction between the neighboring spins, resulting in a coalescence of the hyperfine lines into a sharp single resonance. This is not applicable in our present case, because we have observed an EPR signal with a total width of 1350 G in both $[Mn_2(III,IV)O_2(bipy)_4](ClO_4)_3{\cdot}H_2O$ and $[Mn_2(III,IV)O_2(phen)_4](PF_6)_3{\cdot}CH_3CN$ systems, which have very different counterions. As for the solvent molecules, positions of CH_3CN are not clear in the crystal unit cell of $[Mn_2(III,IV)O_2(phen)_4](PF_6)_3{\cdot}CH_3CN$. Although we cannot go further into a detailed discussion in the present study, the differences of the counterions and solvent molecules between $[Mn_2(III,IV)O_2(bipy)_4](ClO_4)_3{\cdot}H_2O$ and $[Mn_2(III,IV)O_2(phen)_4](PF_6)_3{\cdot}CH_3CN$ may not be eliminated as a possible reason for the significant differences of EPR line width observed in these molecules.

In addition, a small inhomogeneity in the crystal, such as a crystal defect, might also contribute to the line broadening and the anisotropic line width, although we did not observe any significant differences in line broadening among the several crystals of $[Mn_2(III,IV)O_2(phen)_4](PF_6)_3{\cdot}CH_3CN$ that we have examined.

Conclusion

The analysis of orientation-dependent EPR spectra in a single crystal of $[Mn_2(III,IV)O_2(phen)_4](PF_6)_3{\cdot}CH_3CN$ yields precise data on the orientation of the *g* tensor in the molecule and on the anisotropy of the *g* and hyperfine tensors. The anisotropic EPR characteristics of the Mn(III)Mn(IV) system obtained here could be applicable to the precise analysis of the EPR spectra of Mn OEC in PSII, in which 18–20 multiline EPR signals are observed in the S_2 state. It also shows the anisotropic characteristics in membrane samples.[17,61] As observed in the present study, the mixed valence system of Mn(III) and Mn(IV) with oxo-bridged ligands has rhombic g and ^{55}Mn hyperfine couplings, and the relationship of $2A^{IV} = A^{III}$ is not a valid approximation. This could contribute a reason for the origin of more than 16 multiline signals in the OEC S states. However, the total width of the EPR multiline of OEC (~2000 G for S_2 and ~2400 for S_0[62]) is much greater than that of the Mn(III)Mn(IV) di-μ-oxo system (~1350 G). This greater line width cannot be explained by the $2A^{IV} \neq A^{III}$ and *g* and hyperfine anisotropy. It requires other factors such as the presence of more than two manganese in the OEC.

Supplementary Material

Refer to Web version on PubMed Central for supplementary material.

Acknowledgments

This research was supported by a grant from the National Institutes of Health (GM55302) and by the Director, Office of Science, Office of Basic Energy Sciences, Division of Chemical Sciences, Geosciences, and Biosciences, of the U.S. Department of Energy (DOE), under Contract DEAC03-76SF00098. Synchrotron radiation facilities were provided by the Stanford Synchrotron Radiation Laboratory (SSRL), which is operated by the Department of Energy, Office of Basic Energy Sciences. The SSRL Biotechnology Program is supported by the National Institutes of Health, National Center of Research Resources, Biomedical Technology Program, and by the Department of Energy, Office of Health and Environmental Research.

References

1. Khangulov SV, Barynin VV, Antonyukbarynina SV. Biochim. Biophys. Acta. 1990; 1020:25–33.
2. Khangulov SV, Barynin VV, Voevodskaya NV, Grebenko AI. Biochim. Biophys. Acta. 1990; 1020:305–310.
3. Haddy A, Waldo GS, Sands RH, Penner-Hahn JE. Inorg. Chem. 1994; 33:2677–2682.
4. Debus RJ. Biochim. Biophys. Acta. 1992; 1102:269–352. [PubMed: 1390827]
5. Yachandra VK, Sauer K, Klein MP. Chem. ReV. 1996; 96:2927–2950. [PubMed: 11848846]
6. Dismukes GC, Siderer Y. Proc. Natl. Acad. Sci. U.S.A. 1981; 78:274–278. [PubMed: 16592949]
7. Britt, RD. Oxygenic Photosynthesis: The Light Reactions. Ort, DR.; Yocum, CF., editors. Kluwer Academic Publishers; Dordrecht: 1996. p. 137-164.
8. Messinger J, Nugent JHA, Evans MC. W. Biochemistry. 1997; 36:11 055–11 060.
9. Åhrling KA, Peterson S, Styring S. Biochemistry. 1997; 36:13 148–13 152.
10. Messinger J, Robblee JH, Yu WO, Sauer K, Yachandra VK, Klein MP. J. Am. Chem. Soc. 1997; 119:11 349–11 350.
11. Schäfer KO, Bittl R, Zweygart W, Lendzian F, Haselhorst G, Weyhermuller T, Wieghardt K, Lubitz W. J. Am. Chem. Soc. 1998; 120:13 104–13 120.
12. Zheng M, Dismukes GC. Inorg. Chem. 1996; 35:3307–3319. [PubMed: 11666533]
13. Policar C, Knüpling M, Frapart YM, Un S. J. Phys. Chem. B. 1998; 102:10 391–10 398.
14. Randall DW, Sturgeon BE, Ball JA, Lorigan GA, Chan MK, Klein MP, Armstrong WH, Britt RD. J. Am. Chem. Soc. 1995; 117:11 780–11 789.
15. Randall DW, Chan MK, Armstrong WH, Britt RD. Mol. Phys. 1998; 95:1283–1294.

16. Schäfer KO, Bittl R, Lendzian F, Barynin V, Weyhermuller T, Wieghardt K, Lubitz W. J. Phys. Chem. B. 2003; 107:1242–1250.
17. Rutherford AW. Biochim. Biophys. Acta. 1985; 807:189–201.
18. Peloquin JM, Campbell KA, Randall DW, Evanchik MA, Pecoraro VL, Armstrong WH, Britt RD. J. Am. Chem. Soc. 2000; 122:10 926–10 942.
19. Peloquin JM, Britt RD. Biochim. Biophys. Acta. 2001; 1503:96–111. [PubMed: 11115627]
20. Cooper SR, Dismukes GC, Klein MP, Calvin M. J. Am. Chem. Soc. 1978; 100:7248–7252.
21. Tan XL, Gultneh Y, Sarneski JE, Scholes CP. J. Am. Chem. Soc. 1991; 113:7853–7858.
22. Stebler M, Ludi A, Bürgi H-B. Inorg. Chem. 1986; 25:4743–4750.
23. Bencini, A.; Gatteschi, D. EPR of Exchange Coupled Systems. Springer-Verlag; Berlin: 1990.
24. Blondin G, Girerd J-J. Chem. ReV. 1990; 90:1359–1376.
25. Zheng M, Khangulov SV, Dismukes GC, Barynin VV. Inorg. Chem. 1994; 33:382–387.
26. White LK, Belford RL. Chem. Phys. Lett. 1976; 37:553–555.
27. White, LK. Ph.D. Thesis. University of Illinois; Urbana-Champaign: 1975.
28. Robblee JH, Messinger J, Cinco RM, McFarlane KL, Fernandez C, Pizarro SA, Sauer K, Yachandra VK. J. Am. Chem. Soc. 2002; 124:7459–7471. [PubMed: 12071755]
29. Gamelin DR, Kirk ML, Stemmler TL, Pal S, Armstrong WH, Penner-Hahn JE, Solomon EI. J. Am. Chem. Soc. 1994; 116:2392–2399.
30. Pilbrow JR, Winfield ME. Mol. Phys. 1973; 25:1073–1092.
31. Abragam A, Pryce MHL. Proc. Royal Soc. London Ser. A- Math. Phys. Sci. 1951; 205:135–153.
32. Blum H, Salerno JC, Leigh JS Jr. J. Magn. Res. 1978; 30:385–391.
33. Gerritsen HJ, Sabisky ES. Phys. Rev. 1963; 132:1507–1512.
34. This effect is reflected by the longer Mn-ligand bond along the d_z^2 direction in the crystal structure data.
35. The g-values of the tetragonally distorted Mn(III) d^4 system with a $^5B_1$ ground state are described by the following equations,

$$g_{\|}^{\mathrm{III}} = g_e - \frac{8\lambda}{\Delta E_1}$$

$$g_{\perp}^{\mathrm{III}} = g_e - \frac{2\lambda}{\Delta E_2}$$

where g_e is the g value of the free ion (g = 2.0023), ΔE_1 and ΔE_2 the energy difference between the corresponding ground state and the excited state, and λ, the spin–orbit coupling constant for a single d electron.
36. Barra A-L, Gatteschi D, Sessoli R, Abbati GL, Cornia A, Fabretti AC, Uytterhoeven MG. Angew. Chem. 1997; 36:2329–2331.
37. Limburg J, Vrettos JS, Crabtree RH, Babcock GT, de Paula JC, Hassan A, Barra A-L, Duboc-Toia C, Collomb M-N. Inorg. Chem. 2001; 40:1698–1703. [PubMed: 11261982]
38. The g values of a Mn(IV) d^3 system with a $^4A_2$ ground state are described by the following equations,

$$g_{\|}^{\mathrm{IV}} = g_e - \frac{8\lambda}{\Delta E_1'}$$

$$g_{\perp}^{\mathrm{IV}} = g_e - \frac{2\lambda}{\Delta E_2'}$$

where $\Delta E_1'$ and $\Delta E_2'$ are the energy differences between the corresponding ground state and the excited state (see ref 35 for other notations).
39. Geschwind S, Kisliuk P, Klein MP, Pemeika JP, Wood DL. Phys. ReV. 1962; 126:1684–1686.
40. From WH, Dorain PB, Kikuchi C. Phys. ReV. A. 1964; 135:A710–714.
41. Plaksin PM, Stoufer RC, Mathew M, Palenik GJ. J. Am. Chem. Soc. 1972; 94:2121–2122.
42. Jensen AF, Su ZW, Hansen NK, Larsen FK. Inorg. Chem. 1995; 34:4244–4252.

43. Wilson C, Larsen FK, Figgis BN. Acta Crystallogr. Sect. C–Cryst. Struct. Commun. 1998; 54:1797–1799.
44. Baffert C, Collomb M-N, Deronzier A, Pécaut J, Limburg J, Crabtree RH, Brudvig GW. Inorg. Chem. 2002; 52:1404–1411. [PubMed: 11896708]
45. Goodson PA, Glerup J, Hodgson DJ, Michelsen K, Pedersen E. Inorg. Chem. 1990; 29:503–508.
46. Goodson PA, Oki AR, Glerup J, Hodgson DJ. J. Am. Chem. Soc. 1990; 112:6248–6254.
47. In general, elongated Mn–ligandaxial distances are observed along the direction of Jahn–Teller distortion in Mn(III).[33,44] In Mn(III)Mn(III) symmetric compounds, the Mn–N_{axial} distance is close to 2.4 Å, whereas Mn–$N_{equatorial}$ ≈ 2.1 Å.[45] In contrast, the Mn(IV) sites are structurally identical in the Mn(IV)Mn(IV) complex (Mn–N ≈ 2.1 Å).[22,46] The structural distortion at the Mn(III) site in the Mn(III)Mn(IV) complexes is smaller (Mn(III)–N_{axial} ≈ 2.25 Å, Mn(III)–$N_{equatorial}$ ≈ 2.1 Å) [22,41-44] compared with the Mn(III)Mn(III) complexes, suggesting that the unpaired electron is not completely localized in the d_z^2 orbital on the Mn(III) center in the mixed valence system.
48. For the hyperfine coupling constant of the Mn(III) site with $^5B_1$ ground state, the following equations from Abragam and Pryce[31] are applicable:

$$A_{\parallel} = \frac{2\beta\beta_n\gamma}{r^3}\left(-\kappa + \frac{1}{7} + g_{\parallel} - g_e\right)$$

$$A_{\perp} = \frac{2\beta\beta_n\gamma}{r^3}\left(-\kappa + \frac{1}{14} + g_{\perp} - g_e\right)$$

where β is the Bohr magneton; β_n, the nuclear magneton; γ, the nuclear gyromagnetic factor; r, the effective radius of the d shell; and κ, the core polarization parameter. $A_{\parallel}$ is comparable to A_z, while $A_{\perp}$ to $A_{x,y}$.
49. Zhao XG, Richardson WH, Chen JL, Li J, Noodleman L, Tsai HL, Hendrickson DN. Inorg. Chem. 1997; 36:1198–1217. [PubMed: 11669688]
50. McGrady JE, Stranger R. J. Am. Chem. Soc. 1997; 119:8512–8522.
51. Kubo R, Tomita K. J. Phys. Soc. Jpn. 1954; 9:888–919.
52. Van Vleck JH. Phys. ReV. 1948; 74:1168–1183.
53. Bleaney B, Penrose RP, Plumpton BI. Proc. Royal Soc. London Ser. A- Math. Phys. Sci. 1949; 198:406–428.
54. McGregor KT, Soos ZG. J. Chem. Phys. 1976; 64:2506–2517.
55. Hennessy MJ, McElwee CD, Richards PM. Phys. ReV. B. 1973; 7:930–947.
56. Hughes RC, Morosin B, Richards PM, Duffy W. Phys. ReV. B. 1975; 11:1795–1803.
57. Velayutham M, Varghese B, Subramanian S. Inorg. Chem. 1998; 37:5983–5991. [PubMed: 11670731]
58. Gatteschi D, Guillou O, Zanchini C, Sessoli R, Kahn O, Verdaguer M, Pei Y. Inorg. Chem. 1989; 28:287–290.
59. Gloux J, Gloux P, Laugier J. J. Am. Chem. Soc. 1996; 118:11 644–11 653.
60. Felthouse TR, Laskowski EJ, Hendrickson DN. Inorg. Chem. 1977; 16:1077–1089.
61. Kim DH, Britt RD, Klein MP, Sauer K. Biochemistry. 1992; 31:541–547. [PubMed: 1310041]
62. Messinger J, Robblee J, Yu WO, Sauer K, Yachandra VK, Klein MP. J. Am. Chem. Soc. 1997; 119:11 349–11 350.

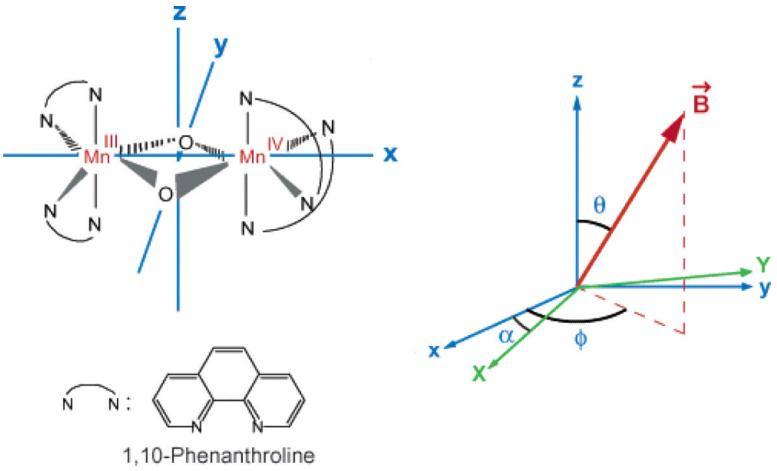

Figure 1.

Geometrical model of the [Mn_2(III,IV)O_2(phen)$_4$] molecule with the definition of the coordinate system used for the g and hyperfine tensors. The Mn_2O_2 unit, which is planar, is in the *xy* plane, with the *x* and *y* axes along the Mn–Mn and the oxo-bridge oxygens, respectively. The *z* axis is perpendicular to the Mn_2O_2 plane. On the right is the coordinate system of the g and hyperfine tensors and the relation to the magnetic field (**B**). θ is the angle between **B** and the *z* axis; φ is the angle of the projection of B in the *xy*-plane; α is the noncoincident angle between the g and hyperfine tensors. The *X* and *Y* axes define the coordinates of the hyperfine tensor when $\alpha \neq 0$ (*z* as the common axis).

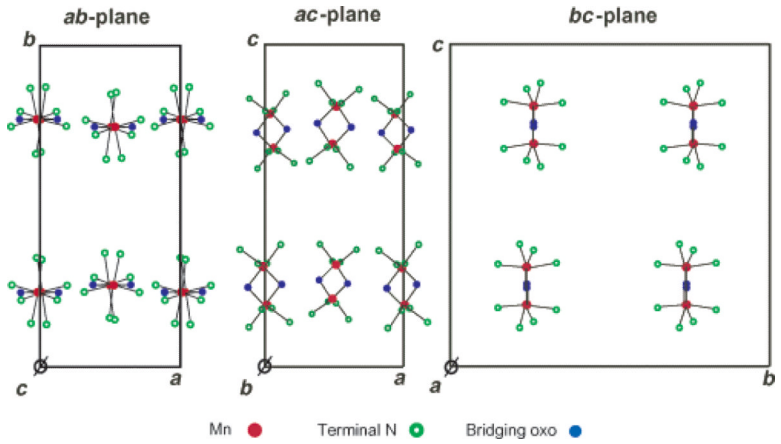

Figure 2.

Molecular arrangement in the crystal unit cell of $[Mn_2(III,IV)O_2(phen)_4](PF_6)_3{\cdot}CH_3CN$; only the Mn, bridging O atoms, and terminal N ligand atoms are shown in the *ab*-, *ac*-, and *bc*-planes.[22] The Mn_2O_2 unit is in the *ac*-plane and the Mn–Mn vector is almost perpendicular to the *ab*-plane.

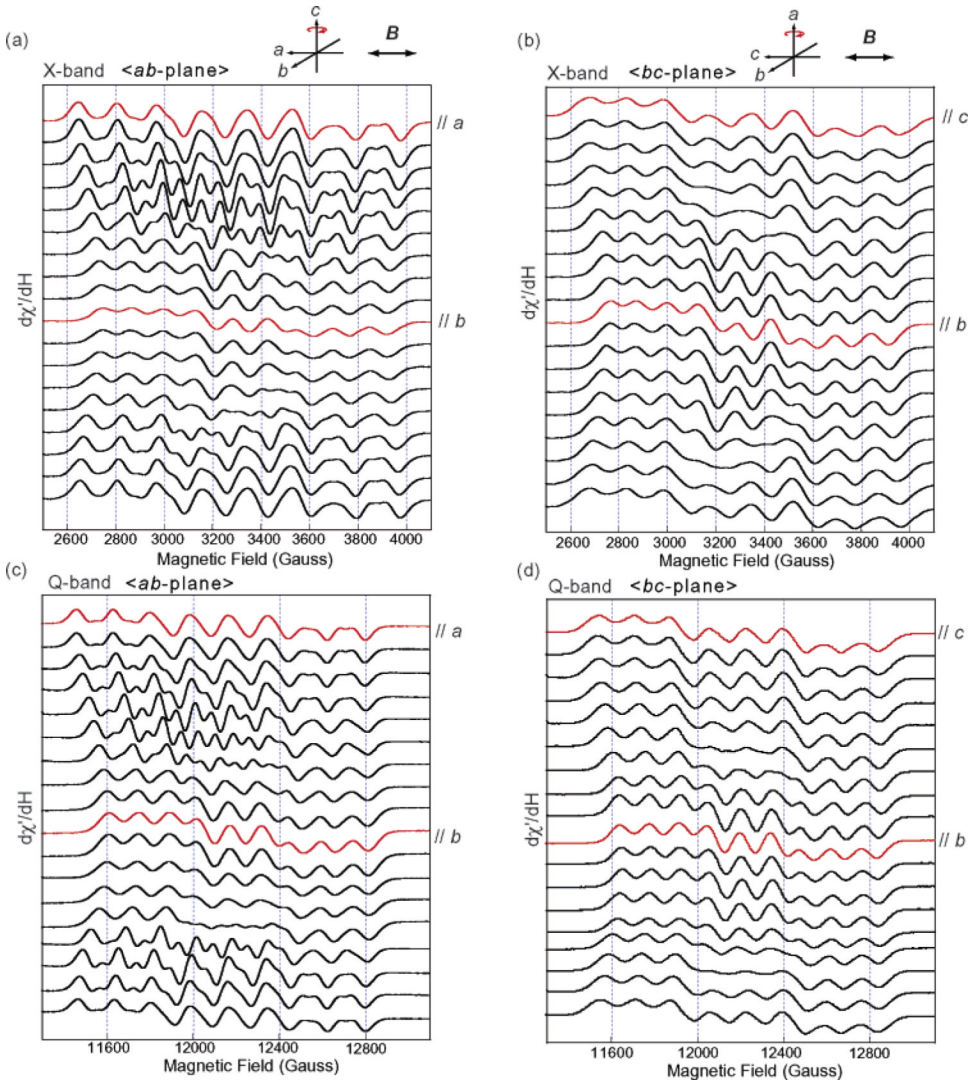

Figure 3.

Angle dependence of the single-crystal EPR spectra of $[Mn_2(III,IV)O_2(phen)_4](PF_6)_3 \cdot CH_3CN$ in the *ab*-plane (a, c) and in the *bc*-plane (b, d). The X-band spectra are shown in (a, b) and the Q-band spectra in (c, d). The spectra were taken at 10° steps from 0° to 170°. The inset on top shows the rotation axis. The spectra in red are the unique spectra with the magnetic field, B, parallel to the *a*, *b*, and *c* axes of the crystal. In the Q-band spectra, slightly different microwave frequencies for individual spectra lead to small shifts of the spectra on the magnetic field axis relative to each other. However, the simulations shown in Figure 4 were carried out using the precise microwave frequencies of the individual spectra.

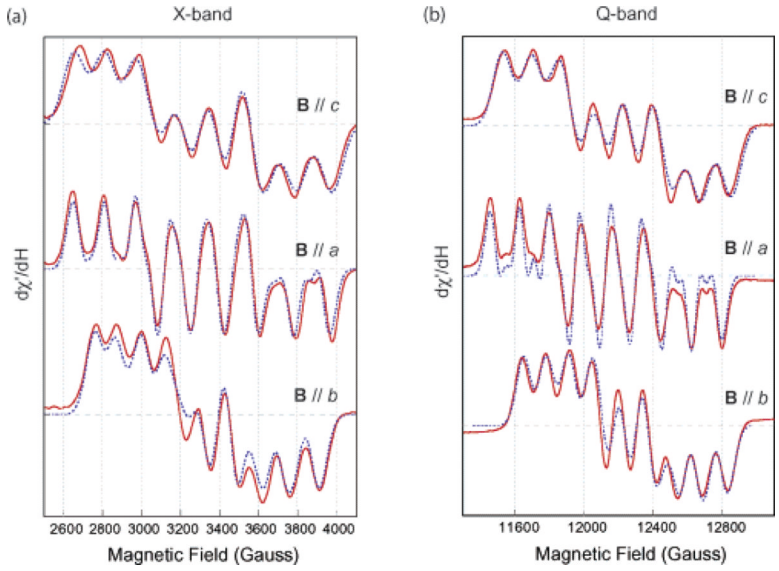

Figure 4.

Simulation of the single-crystal EPR spectra of $[Mn_2(III,IV)O_2(phen)_4](PF_6)_3{\cdot}CH_3CN$ collected at X-band (a) and Q-band frequencies (b). The three experimental spectra are shown as solid lines, and with the magnetic field, B, parallel to each of the crystallographic, *a*, *b*, and *c* axis. Simulations are shown as dotted lines. The best fits for all the single-crystal spectra shown here were obtained with the anisotropic tensors of $g_x = 1.9860$ (±0.0010), $g_y = 1.9935$ (±0.0010), $g_z = 1.9740$ (±0.0008), $A^{III}{}_x = |170\ (\pm 2)|$, $A^{III}{}_y = |176\ (\pm 2)|$, $A^{III}{}_z = |129\ (\pm 2)|$, $A^{IV}{}_x = |76(\pm 2)|$, $A^{IV}{}_y = |75\ (\pm 2)|$, $A^{IV}{}_z = |79\ (\pm 2)|$ G, with the Gaussian line width (HWHM for the absorption spectrum) of 69, 45, and 57 G along the *c*, *a*, and *b*-axes, respectively.

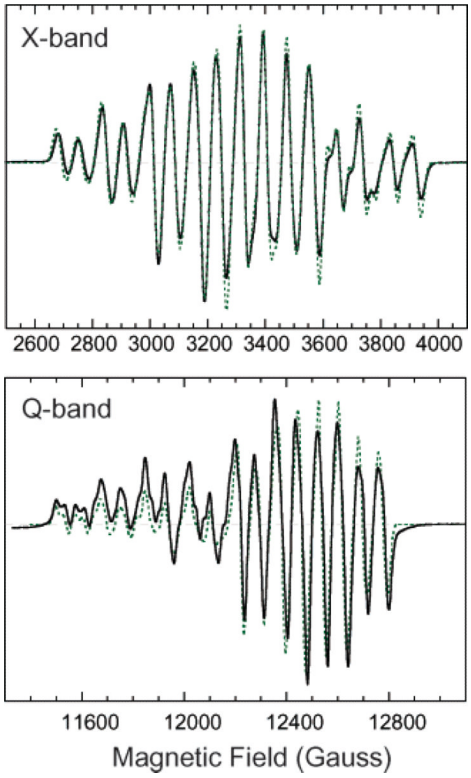

Figure 5.

Solution EPR spectra of $[Mn_2(III,IV)O_2(phen)_4](PF_6)_3{\cdot}CH_3CN$ in acetonitrile (solid lines in black) with the simulation spectra (dotted lines in green); X-band and Q-band. The *g* and hyperfine tensors of the best simulation for both frequencies are $g_x = 1.9887$, $g_y = 1.9957$, $g_z = 1.9775$, $A^{III}{}_x = |171|$ G, $A^{III}{}_y = |176|$ G, $A^{III}{}_z = |129|$ G, $A^{IV}{}_x = |77|$ G, $A^{IV}{}_y = |74|$ G, $A^{IV}{}_z = |80|$ G, with a line width 15 G (HWHM).

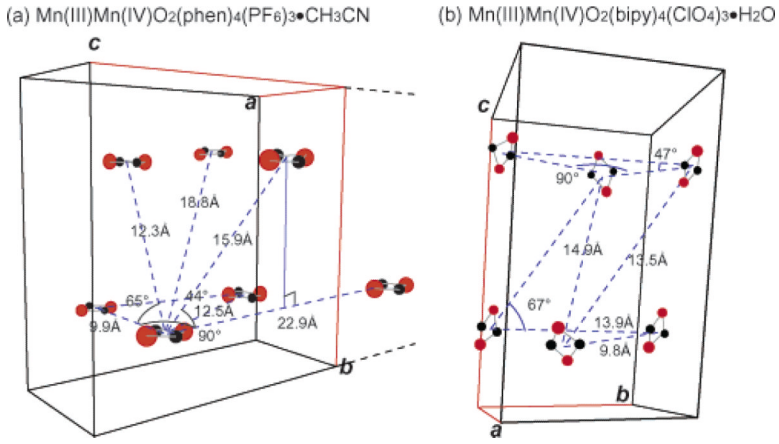

Figure 6.

Molecular arrangement in the unit cell of the crystals of (a) $[Mn_2(III,IV)O_2(phen)_4](PF_6)_3{\cdot}CH_3CN$[22] and (b) $[Mn_2(III,IV)O_2(bpy)_4](ClO_4)_3{\cdot}H_2O$.[42] The distances between the molecules in one unit cell and the relevant nearest molecules in neighboring unit cells are shown. The Mn atoms are in red and the O atoms in black.

Table 1

Orientation of *g*-Tensor Axes of $[Mn_2((III,IV)O_2(phen)_4](PF_6)_3 \cdot CH_3CN$ Molecules in the Single-Crystal[a]

crystal axis	g_x axis parallel to the Mn–Mn vector		g_y axis parallel to the O–O vector		g_z axis perpendicular to the Mn_2O_2 plane
	molecule I	molecule II	molecule I	molecule II	molecule I and II
a	82.8	–82.8	–7.5	7.5	90
b	90	90	90	90	0
c	7.2	–7.2	–82.5	82.5	90

[a]The angles (deg) between the crystallographic *a*, *b*, and *c* axes and the *g*-tensors.[22] I and II are two adjacent molecules in the unit cell of the crystal.

Table 2

g Values and Hyperfine Constants[a] from the Present Single-crystal Study Compared to Other Simulations from EPR and ENDOR Studies Using Solution Spectra

		present study	Schäfer et al.[11]	Randall et al.[15]	Policar et al.[13]
compound		$[(phen)_4Mn_2^{III,IV}(\mu\text{-}O)_2](PF_6)_3\cdot CH_3CN$	$[(phen)_4Mn_2^{III,IV}(\mu\text{-}O)_2](ClO_4)_3\cdot CH_3COCH_3$	$[(phen)_4Mn_2^{III,IV}(\mu\text{-}O)_2](ClO_4)_3\cdot H_2O$	$[(phen)_4Mn_2^{III,IV}(\mu\text{-}O)_2](ClO_4)_3$ *Solvent not specified
form		single-crystal	solution	solution	solution
	g_x	1.9887	1.992	1.995	2.0002[b]
	g_y	1.9957	1.998	1.995	1.9950[b]
	g_z	1.9775	1.98	1.982	1.9814
A^{III}	A^{III}_x	–481 (–171)	–485 (–173)	–480	–495[b]
	A^{III}_y	–493 (–176)	–504 (–178)	–480	–468[b]
	A^{III}_z	–365 (–129)	–387 (–130)	–378	–339
A^{IV}	A^{IV}_x	215 (77)	216 (77)	213	211[b]
	A^{IV}_y	206 (74)	213 (75)	213	211[b]
	A^{IV}_z	227 (80)	230 (84)	229	233

[a] Unit of hyperfine constants: MHz (the values are also given in Gauss in parentheses for the present study and for the reference when the authors reported it in the paper.)

[b] The definition of g_X, g_Y, g_Z in the present study, Schäfer et al.,[11] and Randall et al.[15] are the same with respect to the molecular orientation. The convention $g_X > g_Y > g_Z$ was used in the study of Policar et al.,[13] and the subscripts do not necessarily denote directions in the molecular frame. However, the definition of g_Z is the same as in the other studies.